AGU PUBLICATIONS

JGR

Journal of Geophysical Research: Space Physics

RESEARCH ARTICLE
10.1002/2017JA024305

Key Points:
- Transient perturbations observed in midtail lobe during steady northward IMF interval
- Perturbations are characterized by enhanced pressure and tailward flows, and B_x drops
- MHD simulations suggest that these perturbations are due to Kelvin-Helmholtz vortices

Supporting Information:
- Movie S1

Correspondence to:
C.-P. Wang,
cat@atmos.ucla.edu

Citation:
Wang, C.-P., V. G. Merkin, and V. Angelopoulos (2017), Mesoscale perturbations in midtail lobe/mantle during steady northward IMF: ARTEMIS observation and MHD simulation, *J. Geophys. Res. Space Physics*, *122*, doi:10.1002/2017JA024305.

Received 25 APR 2017
Accepted 13 JUN 2017
Accepted article online 19 JUN 2017

Mesoscale perturbations in midtail lobe/mantle during steady northward IMF: ARTEMIS observation and MHD simulation

Chih-Ping Wang[1], V. G. Merkin[2], and Vassilis Angelopoulos[3]

[1]Department of Atmospheric and Oceanic Sciences, University of California, Los Angeles, California, USA, [2]The Johns Hopkins University Applied Physics Laboratory, Laurel, Maryland, USA, [3]Department of Earth, Planetary, and Space Sciences, University of California, Los Angeles, California, USA

Abstract In this study we investigate an event of sharp and transient (≤10 min) plasma and magnetic field perturbations observed by Acceleration Reconnection Turbulence and Electrodynamics of Moon's Interaction with the Sun (ARTEMIS) probes in the midtail lobe at $X \sim -60\ R_E$. This event occurred under northward interplanetary magnetic field (IMF), and these mesoscale perturbations continued for many hours even as all solar wind and IMF parameters remained steady. The main characteristics of these transient perturbations are as follows: (1) an increase in density and plasma pressure, (2) a drop in B_x, (3) an enhancement in the tailward ($-V_x$) speed, and (4) tailward propagation. We conduct a global magnetohydrodynamic (MHD) simulation for this event using the observed solar wind/IMF conditions. In the simulation, Kelvin-Helmholtz (K-H) vortices are formed at the near-Earth flank and are convected tailward. The K-H vortices have a two-mode structure with the inner mode extending several R_E inside the magnetosphere from the magnetopause. The inner mode vortical flows transport denser mantle plasma from near the magnetopause deeper into the lobe, resulting in localized density and pressure enhancements, while magnetic field changes accordingly with the enhanced flow shear and pressure gradients. As these localized changes pass a fixed location, they create transient perturbations characteristically similar to those observed by ARTEMIS.

1. Introduction

The solar wind-magnetosphere coupling leads to transfer of plasma, momentum, and energy across the magnetopause, and it is this coupling that drives geospace dynamics. For example, the solar wind/magnetosheath plasma can enter the magnetosphere through open magnetic field lines and form mantle plasma in the lobes. With increasing tail distances, magnetic field in the magnetosphere becomes weaker while the shocked magnetosheath flow returns to being more solar wind like. Therefore, the magnetopause dynamics becomes dramatically different from that in the near-Earth region. This has been shown by earlier ISEE 3 and Geotail observations in the distant tail beyond 100 R_E [e.g., *Gosling et al*., 1984; *Maezawa and Hori*, 1998; *Hasegawa et al*., 2002], and by recent Acceleration Reconnection Turbulence and Electrodynamics of Moon's Interaction with the Sun (ARTEMIS) observations in the midtail at ~60 R_E [e.g., *Wang et al*., 2014]. For example, mantle plasma was found to appear at lower latitudes and become more dawn-dusk asymmetric as interplanetary magnetic field (IMF) B_y becomes more dominant. The subsequent transfer of mantle plasma into the closed field line region through magnetotail reconnection plays an important role in shaping the plasma sheet properties, and the reconnection process is significantly affected by mantle plasma distributions above and below the tail current sheet [e.g., *Hietala et al*., 2015, 2017].

Wang et al. [2014] showed statistically that mantle plasma flows tailward along the lobe magnetic field lines while drifting toward midnight and the tail current sheet and that mantle density decreases with increasing cross-tail distances away from the magnetopause. However, sometimes the drift and density were found to be highly fluctuating at mesoscale (a few to tens of minutes) with fluctuation magnitudes significantly larger than the averages. To better understand these mesoscale fluctuations in mantle plasma, in this study we investigate an event of the midtail lobe/mantle under prolonged northward IMF, during which the two Acceleration Reconnection Turbulence and Electrodynamics of Moon's Interaction with the Sun (ARTEMIS) probes observed a sequence of sharp and transient changes in plasma and magnetic field. We chose this particular event for its rather steady conditions in all the solar wind and IMF parameters so that the perturbations were less likely to be originated in the solar wind. We also conduct global magnetohydrodynamic

(MHD) simulations of this event using Lyon-Fedder-Mobarry (LFM) model to help interpret the physical processes behind these perturbations.

2. ARTEMIS Observation

Measurements in the midtail are from the two ARTEMIS probes, P1 and P2 [*Sibeck et al*., 2011], which were located at lunar distances ($r \sim 60\ R_E$) at the time. We use the spin-fit magnetic field vectors measured by the fluxgate magnetometer (FGM) instrument [*Auster et al*., 2008] and onboard ion fluxes and plasma moments measured by the electrostatic analyzer (ESA, 0.006–20 keV/q for ions and 0.007–26 keV for electrons) [*McFadden et al*., 2008]. The solar wind/IMF conditions are from OMNI data that have been shifted to the Earth's bow shock nose [*King and Papitashvili*, 2005].

The event for this study occurred from 03:00 to 07:00 UT on 13 February 2014, which was within a very long interval of northward IMF (over 2 days) that started at ~16:00 UT on 12 February 2014. We only focus on this 4 h interval for its relatively steady solar wind/IMF conditions. IMF B_z was ~+3.5 nT, and IMF B_y was ~−4 nT. As shown in Figure 1a, fluctuations in all solar wind and IMF parameters were very small. This OMNI IMF conditions were consistent with the magnetic fields observed by Geotail, which at the time was just upstream of the bow shock at ~(28, 4, and 11) R_E (not shown). In the midtail, the two ARTEMIS probes had crossed the duskside magnetopause approximately a day earlier at ~04:00 UT on 12 February 2014 and since then moved in the northern lobe. Figure 1b shows that the probes moved inward from Y_{AGSM} ~18 to ~15 R_E during the event (AGSM is aberrated geocentric solar magnetospheric coordinates). As they moved, their alignment kept changing and their separation varied between ~1 and 3 R_E. The magnetic fields, omnidirectional ion energy fluxes, and ion plasma moments observed by P2 are shown in Figure 1c. B_x was mostly positive, indicating that P2 was in the northern lobe. For most of the event, P2 observed ions with substantial density ($>$0.2 cm^{-3}) and field-aligned tailward flows (<-100 km/s; see $V_{\|,x}$ indicated by the green line). These characteristics indicate that it was mantle plasma [*Wang et al*., 2014]. In contrast to the steady IMF and solar wind conditions, sharp and transient changes in magnetic fields and plasma, as marked by the red vertical dotted lines, occurred repetitively in the lobe. We identify each change with a criterion that B_x dropped to below the 4 h B_x average (~3 nT) and recovered within 10 min. There were total 29 such transient changes observed by the two probes within the 4 h interval. The interval between two changes varied from a few to tens of minutes. For each B_x drop, there was an enhancement in the fluxes of colder ions ($<$~1 keV).

Figure 2a shows an example of these transient changes. We conduct superposed epoch analysis of all the 29 changes. We define $t = 0$ as the time when B_x dropped to its minimum. For each parameter, we compute the deviations from the 10 min average within $t = -5$ to +5 min. Figure 2b shows quartiles of these deviations. The main characteristics of the transient changes include the following:

1. A drop in B_x. For some of the drops the B_x direction changed from positive to negative. B_y and B_z fluctuated, and their changes were substantially smaller than the B_x change.
2. An increase in density and plasma pressure.
3. An enhancement in the tailward ($-V_x$) speed. The speed changes in V_y and V_z were smaller than those in V_x. The V_y direction often changed from negative to positive.

In addition, Figure 2a also shows that P2 observed the transient change earlier than P1, indicating that the change was propagating from P2 to P1. Figure 2c shows that P1 and P2 at the time were mainly separated in the X direction. P2 was about 1.5 R_E earthward of P1, and it observed the sharp B_x drop ~35 s earlier (see the two vertical dotted lines in the B_x plot of Figure 2a). Considering that the transient change seen by P2 lasted for about 4 min, it is estimated that the X scale of the transient change was ~10 R_E and it moved at a tailward speed of ~270 km/s.

3. Simulation

To investigate the likely physical processes responsible for the observed mesoscale plasma and magnetic field perturbations in the lobe, we conduct a simulation for this event using 3-D LFM global magnetosphere MHD model using the observed solar wind/IMF conditions as the upstream boundary conditions. This simulation is one of the simulation runs using different global MHD models conducted for "Midtail Modeling Challenge" on the NASA Community Coordinated Modeling Center.

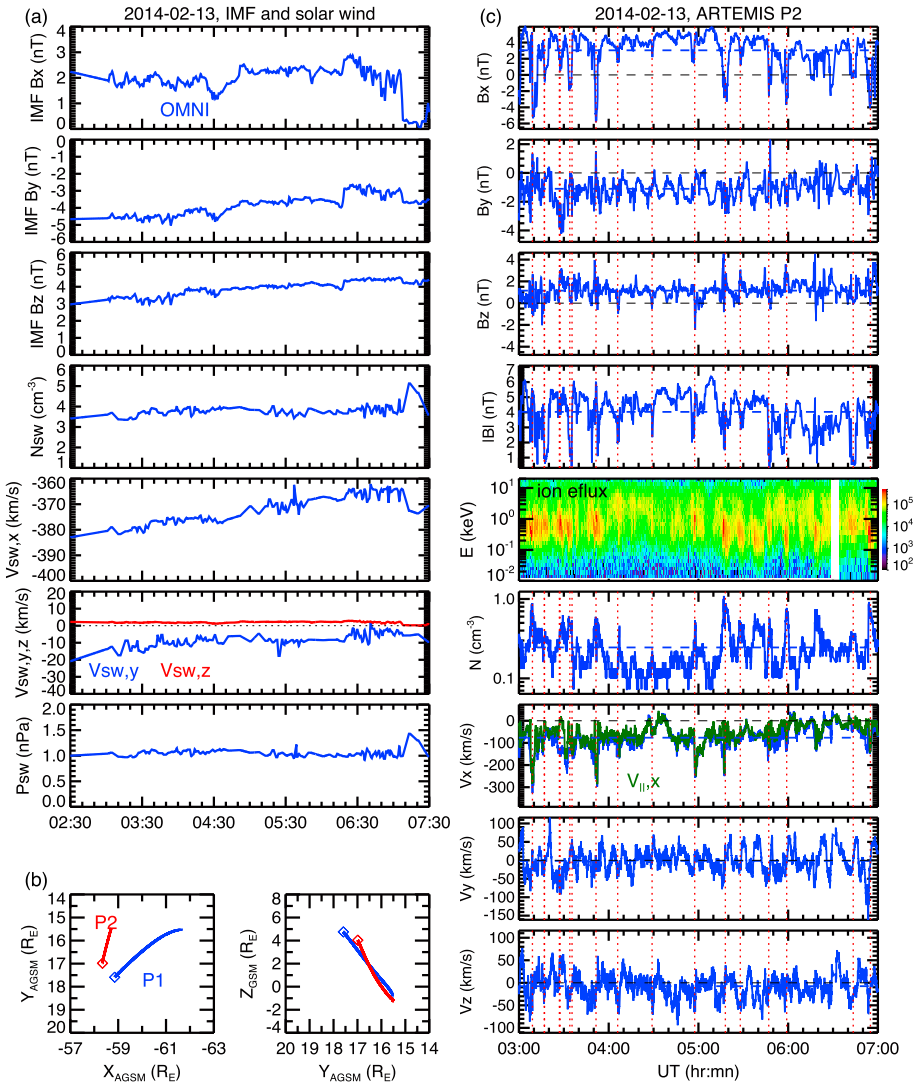

Figure 1. (a) OMNI solar wind and IMF. (b) *X-Y* and *Y-Z* projection of the trajectories of the two ARTEMIS probes from 02:30 to 07:30 UT (the squares indicate the locations at 02:30 UT). (c) From top to bottom: magnetic field components, ion energy fluxes, number density, and bulk flow velocities observed by ARTEMIS P2.

3.1. Simulation Setup

The LFM global magnetosphere MHD model [*Lyon et al.*, 2004] was run at a high resolution. The LFM magnetospheric code uses a distorted spherical grid whose symmetry axis is aligned with the Solar Magnetic (SM) *X* axis. The grid had 212 grid cells in the radial dimension, 256 in the azimuthal dimension, and 192 in the polar dimension. The cell sizes are highly variable; at the terminator (that is, the $X = 0$ plane) magnetopause the radial cell size is ~0.1 R_E (and further refined at the dayside), while at $X = -50$ R_E it is ≤ 1 R_E. The outer boundary of the simulation grid is a cylinder of radius 124 R_E extending from $X_{SM} = 30$ to -330 R_E. The inner boundary is located at 2 R_E. The outer boundary condition was set in accordance with the upstream solar wind and IMF conditions obtained from OMNI, and the simulation was run with these upstream conditions from 03:00 to 08:00 UT. All the subsequent analysis was done between 05:00 and 08:00 UT such that the simulated magnetosphere was allowed sufficient preconditioning prior to the beginning of analysis. The inner boundary condition is obtained from the electrostatic potential solution using the Magnetosphere-Ionosphere Coupler Solver (MIX) code [*Merkin and Lyon*, 2010]. The ionospheric conductance was calculated by the empirical model which first computes the extreme ultraviolet ionization contribution and then estimates the precipitating electron characteristic energy and flux from MHD variables [*Fedder et al.*, 1995; *Wiltberger et al.*, 2009].

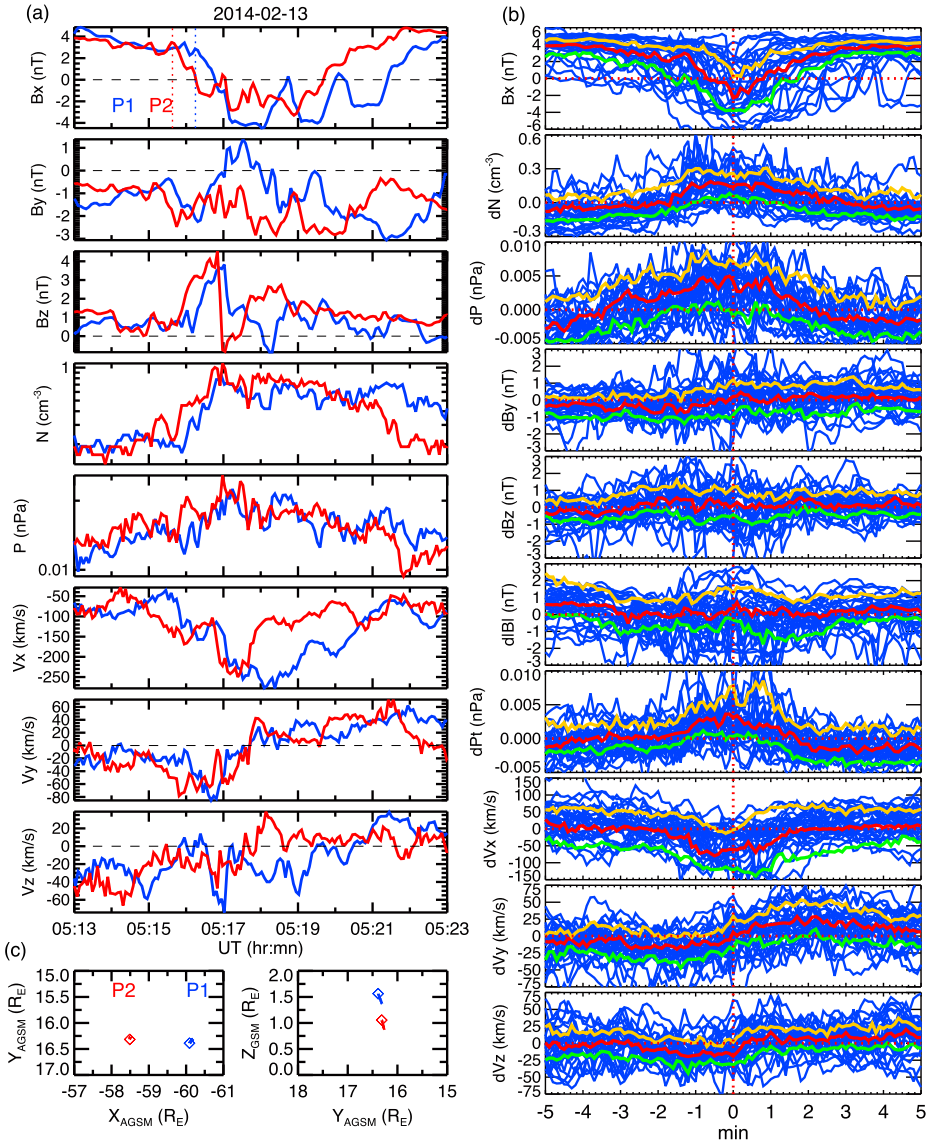

Figure 2. (a) From top to bottom: magnetic fields, number density, ion pressure, and ion bulk velocities observed by P1 (blue) and P2 (red). (b) Superposed epoch analysis of changes in plasma and magnetic fields associated with the transient B_X change. The green, red, and yellow curves indicate the 25%, 50%, and 75% quartiles, respectively. (c) *X-Y* and *Y-Z* projection of the trajectories of the two ARTEMIS probes from 05:13 to 05:23 UT.

3.2. Mesoscale Pressure Enhancement and B_x Reduction

The simulation results are presented in geocentric solar magnetospheric (GSM) coordinates GSM. The *Y-Z* distributions of simulated B_x, plasma pressure (P), and V_x at $X = -55\ R_E$ at 06:57 UT are shown in Figure 3a. The northern lobe ($B_x > 0$) and the southern lobe ($B_x < 0$) are separated by the cross-tail current sheet (indicated by the black dotted curves). Plasma in the current sheet flows earthward and has significantly higher plasma pressure than the lobes. *Y-Z* projections of several open field lines (the white curves in the B_x plot) across different (Y, Z) locations at $X = -55\ R_E$ (indicated by the white dots) are overplotted in the B_x plot. These field lines indicate that the tail magnetopause is open on the duskside in the northern lobe and on the dawnside in the southern lobe. A dawn-dusk asymmetry with higher pressure on the duskside (dawnside) in the northern (southern) lobe is contributed by mantle plasma entering through the open magnetotail magnetopause. This dawn-dusk asymmetry has been observed in the midtail [*Wang et al.*, 2014]. In the presence of IMF B_y, the magnetosphere shape in the *Y-Z* plane becomes more elliptical with increasing downtail distances. The long axis of the ellipse is aligned with the IMF B_{yz} orientation. This configuration is due to the

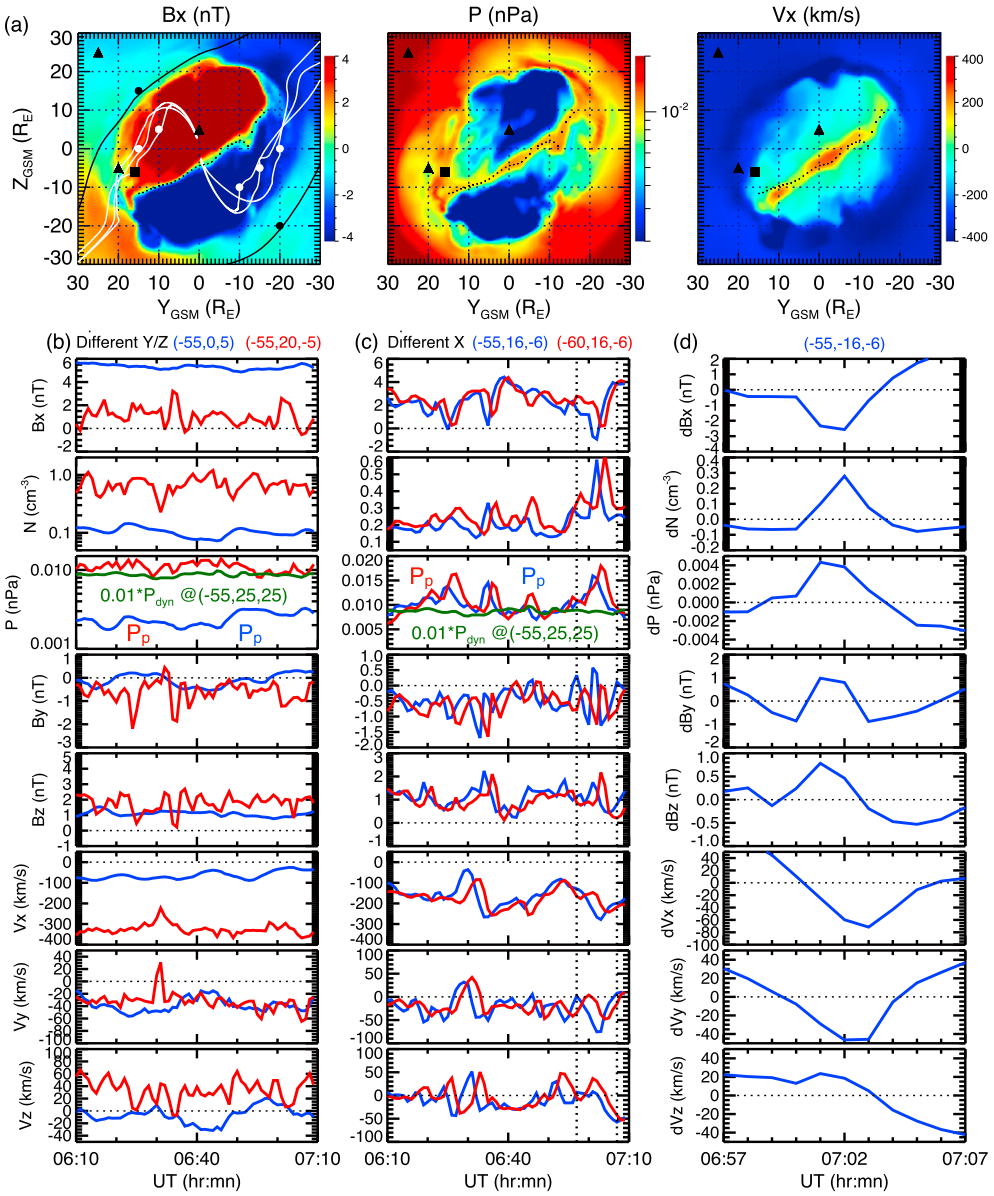

Figure 3. (a) *Y-Z* profiles of simulated B_x, plasma pressure, and V_x at $X = -55\ R_E$ at 06:57 UT (the dotted curves indicate the cross-tail current sheet). The black curves in the B_x plot are IMF magnetic field lines across the black dots, and white curves are open magnetic field lines across the white dots. Comparisons of the temporal profiles of simulated parameters at two lobe locations at (b) the same *X* but different *Y/Z* and (c) the same *Y/Z* but different *X* (locations indicated by the black triangles in Figure 3a). The green lines are scaled dynamic pressure in midtail magnetosheath. (d) Deviations in the simulated parameters at (−55, 16, and −6) (indicated by the black square in Figure 3a) from their 10 min averages associated at the B_x change R_E at 07:02 UT.

dawn-dusk asymmetry in the open magnetopause and magnetic tension force of draped magnetosheath magnetic field lines (as indicated by the black lines in the B_x plot of Figure 3a) in the presence of IMF B_y [*Sibeck and Lin*, 2014]. The current sheet is also tilted from the constant *Z* plane, and the tilt angle becomes larger with increasing downtail distances.

Figure 3b compares the temporal variations of magnetic field and plasma parameters at two lobe locations at $X = -55\ R_E$: one at midnight ($Y = 0$ and $Z = 5\ R_E$) and one near the magnetopause ($Y = 20$ and $Z = -5\ R_E$). At the midnight location, which is deep within the magnetosphere, both plasma and magnetic fields remain relatively steady. In contrast, large fluctuations with periods of ~5–10 min are seen near the magnetopause. Figure 3c shows results at $Y = 16$ and $Z = -6\ R_E$ at two different *X* locations ($X = -55$ and $-60\ R_E$). We

choose this (*Y*, *Z*) location because the overall magnitudes of magnetic field components and plasma moments are similar to the ARTEMIS observations shown in Figure 1c. Transient changes in magnetic fields and plasma pressure with tens of minutes separation between two changes are seen at this location, similar to the ARTEMIS observations. As shown in Figure 1a, the observed solar wind dynamic pressure, which is used as the upstream conditions in this simulation, was fairly steady. To check that there are also no large fluctuations in the magnetosheath, in the pressure plots of Figures 3b and 3c we also show the simulated magnetosheath dynamic pressure at (−55, 25, and 25) (the green lines) in comparison with the plasma pressures inside the magnetosphere (shown in blue and red; note that the magnetosheath dynamic pressure has been multiplied by a scale factor of 0.01 for better visual comparisons with the plasma pressures). This comparison shows that the large perturbations inside the magnetosphere are not due to magnetopause compression by fluctuations in the solar wind and magnetosheath dynamic pressures [e.g., *Li et al*., 2011]. Among the fluctuations shown in Figure 3c, the B_x drop at 07:02 UT at $X = -55\ R_E$ is particularly large with a change in the B_x direction. This drop is the main focus of the simulation results presented below. Deviations of different parameters from their 10 min averages associated with this transient B_x change from 06:57 to 07:07 UT are shown in Figure 3d. The B_x reduction is correlated with enhancements in density, plasma pressure, and tailward speed and a change in the V_y direction. These changes are consistent with the characteristics of the observed transient changes shown in Figures 2a and 2b. The magnitudes of these deviations are also comparable with the observed ranges. In addition, Figure 3c shows that the changes occur at $X = -55\ R_E$ earlier than at $X = -60\ R_E$, indicating tailward propagation of these perturbations, consistent with the ARTEMIS observations shown in Figures 2a and 2c.

To investigate the transient change seen at (−55, 16, and −6) R_E at 07:02 UT shown in Figure 3d, we plot in Figure 4 spatial distributions of B_x and P in the *Y*-*Z* plane at $X = -55\ R_E$ at three different moments from 06:57 to 07:03 UT, as well as in the *X*-*Y* plane at $Z = -7\ R_E$. Movie S1 in a format similar to Figure 4 is included in the supporting information and is intended to get the reader a better sense of the evolution of the transient change. The time sequence shows that the transient change is due to a localized structure of reduced B_x and enhanced P moving tailward. The structure is ~5 R_E in the *Y* and *Z* directions and $\gtrsim$10 R_E in the *X* direction. The elongated structure extends inward several R_E into the lobe from the magnetopause with an alignment along the $+X$ and $-Y$ direction. As it extends inward, the structure is well separated from the cross-tail current sheet (indicated by the dashed curves) so that the transient change is not due to crossing of the equatorial current sheet.

3.3. Flow Vortices and Pressure Enhancement

To understand where plasma within the pressure enhancement comes from, we trace a fluid element from (−55, 15, and −7) R_E backward in time from 07:03 UT. The tracing is conducted in the time-dependent 3-D velocity field at 1 min cadence, and linear interpolation is used for obtaining velocities between grid points. We also traced the magnetic field lines across that element at different times to determine whether the element was inside or outside the magnetosphere. The trajectory of this element, shown in Figure 5a, indicates that it came from the solar wind and entered the magnetosphere at ~(−4, 14, and −11) R_E at 06:44 UT. It then moved tailward in the lobe adjacent to the magnetopause at speed of up to ~300 km/s and thus became part of mantle plasma. It reached $X \sim -35$ and $Y \sim 20\ R_E$ at 06:55 UT and started to move inward while still moving tailward at a speed of ~230–280 km/s. Therefore, the transient change is contributed by mantle plasma that penetrates deeper into the magnetosphere. For comparison, we also trace another fluid element backward in time starting at the same location but from an earlier time at 06:53 UT before the transient change. The trajectory, as shown in Figure 5b, indicates that it meandered slowly within the lobe region between $X = -40$ and −60 and $Y = 10$ and 20 R_E for the past 2 h. Therefore, the plasma within the transient change has quite a different transport path from the plasma before the change.

To understand how mantle plasma from near the magnetopause is able to penetrate deeper into the lobe in a sharp and transient manner, we investigate the spatial and temporal variations of velocity fields. We define the temporal perturbations of velocity as $\delta\mathbf{V} = \mathbf{V} - \langle\mathbf{V}\rangle$, where $\langle\mathbf{V}\rangle$ is the average within the 3 h simulation period. Figure 5c shows 2-D streamlines of δV_x and δV_y at different times and in different areas following the mantle fluid element shown in Figure 5a. Note that the *X* ranges for different columns are different so that the streamlines can be more clearly shown. The mantle element is at the outer edge

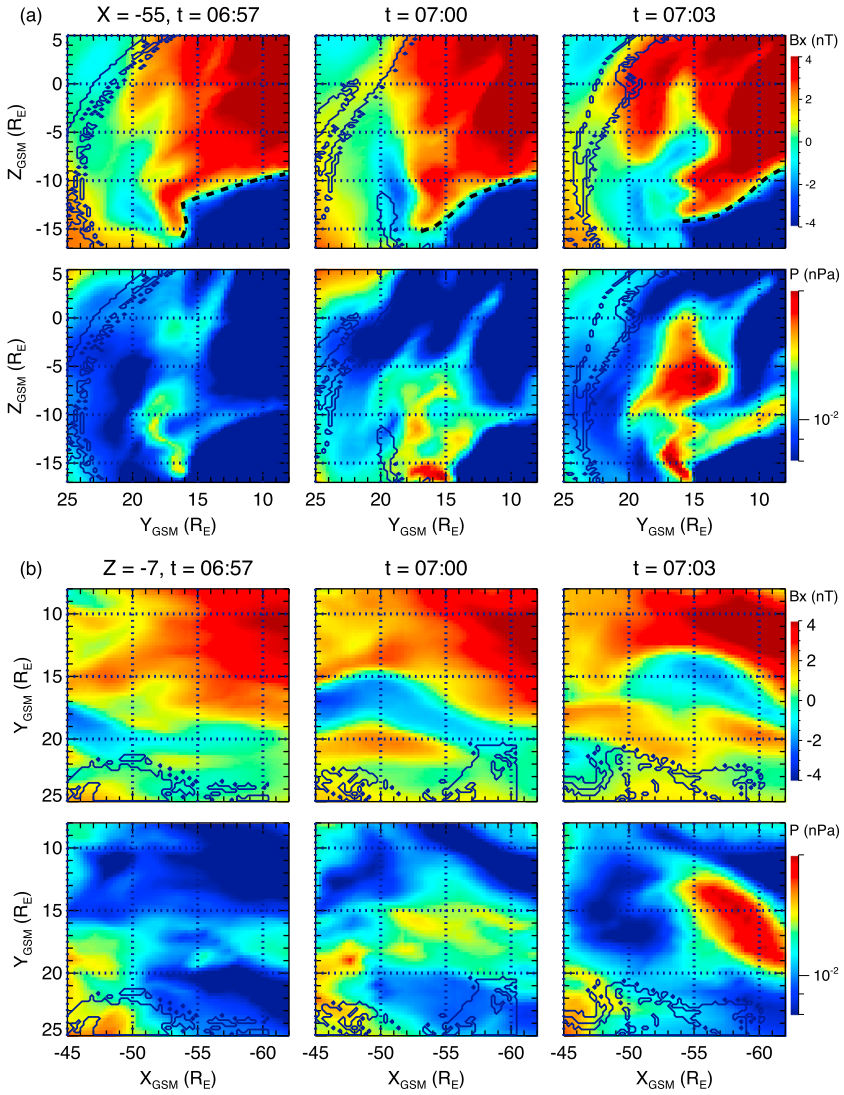

Figure 4. (a) *Y-Z* profiles of simulated B_x (top row) and plasma pressure (bottom row) at $X = -55\ R_E$ at 06:57 (left), 07:00 (middle), and 07:03 UT (right) (the black dashed curves indicate the cross-tail current sheet). (b) *X-Y* profiles of simulated B_x (top row) and plasma pressure (bottom row) at $Z = -7\ R_E$ at 06:57 (left), 07:00 (middle), and 07:03 UT (right).

of a vortex that rotates counterclockwise (as viewed from +*Z*). The scale of the vortex is ~10 R_E in *X* and ~5 R_E in *Y*. The vortex is inside the magnetosphere, and its center is several R_E from the magnetopause. The vortex is moving tailward at a speed varying from ~250 to 300 km/s. This speed is comparable with the speed estimated from the observations shown in Figures 2a and 2c. The fluid element was initially near the magnetopause and in the ($\delta V_x < 0$ and $\delta V_y \sim 0$) portion of the vortex, so that it moved mainly tailward. After ~06:55 UT, it was caught up in the $\delta V_y < 0$ portion of the vortex and started to move inward substantially. Figure 5d shows streamlines in the *Y-Z* plane at $X = -46\ R_E$ at 07:00 UT. The *Z* scale of the vortex is ~5 R_E. Figure 5e shows a 3-D view of one of the streamlines at the moment of 07:00 UT, and it shows that the vortex axis is tilted from the *Z* axis. Therefore, mantle plasma brought deeper into the lobe by the negative δV_y flow of the mesoscale vortex results in the localized and elongated structure of enhanced plasma pressure as shown in Figure 4.

Figure 6a shows the spatial distribution of V_y in the $Z = -7\ R_E$ plane at 06:47 UT. A train of localized regions of negative V_y, each associated with a flow vortex, is seen distributed along the magnetopause from dayside to the midtail. Therefore, as they propagate tailward, they repetitively cause sharp and transient change at a fixed location as seen in the ARTEMIS observations. Figure 6b shows vectors of

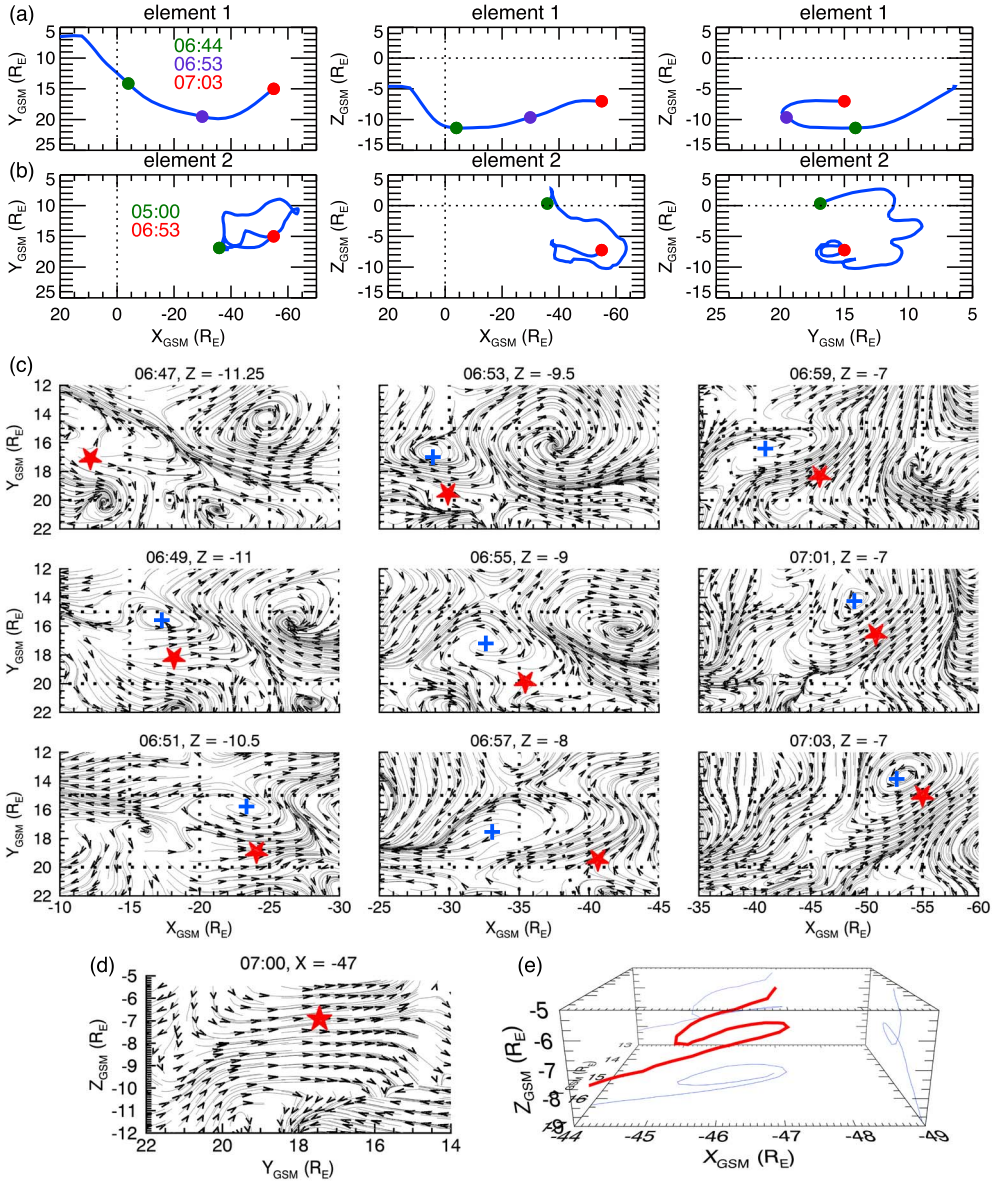

Figure 5. Backward tracing of a fluid element from the location (−55, 15, and −7) R_E starting at (a) 07:03 UT and (b) 06:53 UT. (c) 2-D streamlines of velocity perturbations, δV_x and δV_y, at different times and different Z. The red stars indicate the locations of the fluid element shown in Figure 5a, and the blue crosses indicate the center of the counterclockwise vortex. (d) 2-D streamlines of δV_y and δV_z at $X = -55$ R_E at 07:00 UT. (e) A 3-D view of a δV streamline at 07:00 UT. Projections of the streamline onto different planes are shown in light blue.

δV_x and δV_y in the near Earth at 06:44 UT (the time the fluid element 1 shown in Figure 5a entered the magnetosphere). Several flow vortices were present. Vortices 1 and 2 were adjacent to the magnetopause (outer layer), while vortices 3, 4, and 5 were located a few R_E from the magnetopause (inner layer). This feature of double-vortex layers has been reported previously in global MHD simulations [e.g., *Merkin et al.*, 2013], and they were shown to be associated with Kelvin-Helmholtz (K-H) surface waves. As shown in Figure 6c, the double-vortex layers are also seen in the midtail, suggesting that the double-vortex layer structure remained intact as these vortices were convected tailward. It is these inner vortices that bring mantle plasma deep into the lobe. Comparing Figures 6b and 6c indicates that the Y scale of these vortices grows as they propagate tailward, allowing for deeper penetration of mantle plasma farther down the tail.

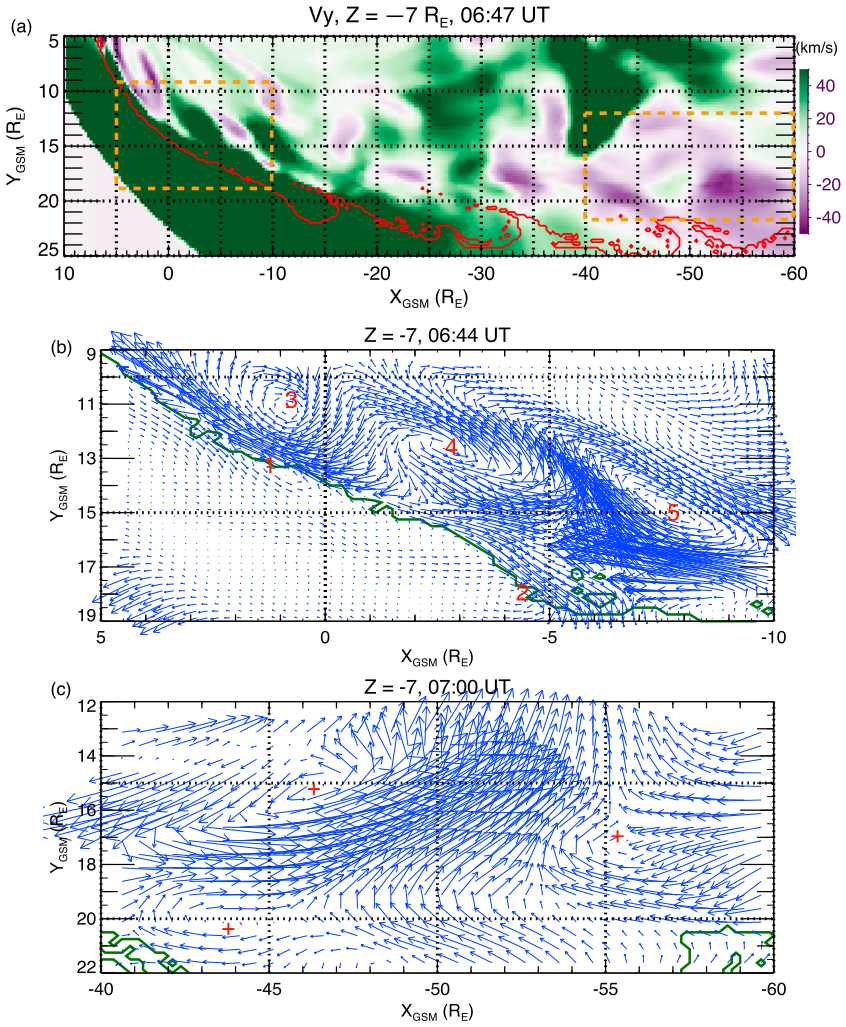

Figure 6. (a) *X-Y* distributions of simulated V_y at $Z = -7\ R_E$ at 06:47 UT. The red curve indicates the magnetopause, and the two orange rectangles indicate the regions shown in Figures 6b and 6c. Vectors of δV_x and δV_y at $Z = -7\ R_E$ in (b) near-Earth region at 06:44 UT and (c) midtail at 07:00 UT. The green curves indicate the magnetopause. The red numbers and the red crosses indicate the centers of vortices.

3.4. Force Balance and B_x Reduction

Considering the four force terms in the MHD momentum equation, $\rho\partial\mathbf{V}/\partial t$, $\rho\mathbf{V}\cdot\nabla\mathbf{V}$, ∇P, and $\mathbf{J}\times\mathbf{B}$, where ρ is the mass density and $\mathbf{J}$ is current density, the moving vortices contribute to $\rho\partial\mathbf{V}/\partial t$ and their flow shears contribute to $\rho\mathbf{V}\cdot\nabla\mathbf{V}$, while the localized plasma pressure enhancements generate a strong ∇P. Figure 7 shows the Y profiles of P, $\mathbf{V}$, $\mathbf{B}$, $\mathbf{J}$, and the four force terms at 07:03 UT at $Z = -6$ and $X = -58\ R_E$. This (X, Z) location at the time was near the peak of the tailward moving pressure enhancement. The P peak was at $Y \sim 14\ R_E$, and a strong ∇P in the Y direction was generated in the inner edge of the pressure enhancement ($Y \sim 12$–$14\ R_E$) shown in Figure 7f, where both $\rho\partial\mathbf{V}/\partial t$ and $\rho\mathbf{V}\cdot\nabla\mathbf{V}$ were too small to balance it. The strong ∇P was mainly balanced by $\mathbf{J}\times\mathbf{B}$ that was associated with the sharp B_x change between $Y \sim 12$ and $14\ R_E$. In the outer edge of the pressure enhancement ($Y \sim 14$–$18\ R_E$), in the Y direction ∇P was comparable to $\rho\mathbf{V}\cdot\nabla\mathbf{V}$. But in the X direction $\rho\mathbf{V}\cdot\nabla\mathbf{V}$ was much stronger than ∇P, and a sharp B_x change rose at the outer edge between $Y \sim 16$ and $18\ R_E$. As a result, a localized B_x dip was formed in correspondence to the pressure peak.

4. Discussion

One of the interesting questions that our findings shed new light on is whether the magnetospheric boundary at these relatively large tail distances exhibits K-H fluctuations. K-H instability and associated flow vortices

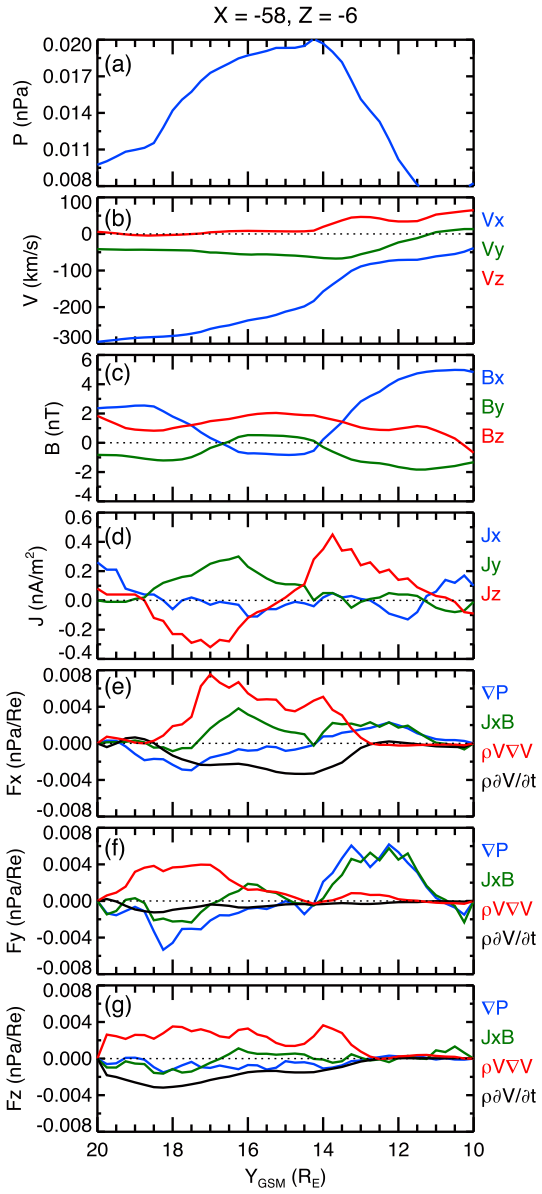

Figure 7. *Y* profiles of (a) plasma pressure, (b) plasma velocity components, (c) magnetic field components, (d) current density components, and force components in the (e) *X*, (f) *Y*, and (g) *Z* directions at 07:03 UT at $X = -58$ and $Z = -6$ R_E.

at the magnetopause have been observed before at much closer distances to the Earth [e.g., *Hasegawa et al.*, 2004; *Taylor et al.*, 2012; *Lin et al.*, 2014]. Recent global MHD simulations have reproduced the magnetopause oscillations as well [*Li et al.*, 2012; *Merkin et al.*, 2013] and suggested that the boundary can be perturbed farther into the tail, although the wave power of the oscillations peaks near the terminator [e.g., *Merkin et al.*, 2013]. These previous simulations only focused on the flank magnetopause closer to the Earth ($r < \sim 40$ R_E). The simulation presented in this paper is the first one to investigate the magnetopause perturbations in midtail. It is interesting to point out that the simulation results presented herein do not necessarily mean that the velocity shear at the magnetospheric boundary is K-H unstable at such large distances in the tail. The perturbations that are excited closer to Earth become nonlinear and saturate rather quickly [*Merkin et al.*, 2013] and then are convected down the tail while growing in size spatially. The plasma and field oscillations in the midtail reported above are possible signatures of such convecting structures. Several global simulations have investigated how the K-H instability is excited at the near-Earth magnetopause under different solar wind and IMF conditions [e.g., *Hwang et al.*, 2011; *Li et al.*, 2011; *Merkin et al.*, 2013]. However, it remains to be understood how the solar wind/IMF conditions may affect evolution of K-H vortices as they are convected to midtail. More detailed analyses, including both observations and modeling, will need to be carried out to investigate these questions further.

The mesoscale perturbations in the mantle shown in this study could have consequences for magnetotail reconnection. In the magnetotail, the appearance of mantle plasma in the northern and southern lobes is strongly affected by IMF B_y [e.g., *Wang et al.*, 2014]. For example, IMF B_y was ~ −4 nT in this event and Figure 3a shows that mantle plasma in the dusk sector appears mainly in the northern lobe; thus, plasma density and pressure are higher above the current sheet than below the current sheet. This distribution suggests that the plasma conditions in the inflow region of reconnection above and below the current sheet are different, an asymmetry that is expected to affect the reconnection process [e.g., *Cassak and Fuselier*, 2016]. *Hietala et al.* [2015, 2017] used ARTEMIS observations to investigate the midtail current sheet near the dusk flank and found that the plasma and magnetic field properties in the outflow region of

reconnection are affected by this inflow asymmetry. For example, the outflow jet is marginally firehose stable in an asymmetric case but highly unstable in a symmetric case. MHD simulations showed that under steady electric drift in the lobes, which is pointed inward and toward the current sheet, the resulting mantle density is the highest at the magnetopause and decreases monotonically with increasing cross-tail distances from the magnetopause| [*Wang et al.*, 2014], suggesting that the asymmetric inflow condition is weaker farther inside the magnetosphere. However, the simulations in this study show that inward protrusion of mantle plasma by the K-H flow perturbations can result in localized enhancement of mantle plasma density, thus a more asymmetric inflow condition (by a factor of up to ~2), at a location deeper inside the magnetosphere than can be produced by steady drift. How the reconnection process across the magnetotail would be affected by these mesoscale temporal and spatial perturbations in the inflow conditions and how the resulting plasma sheet would be different from that without the perturbations should be further investigated in the future.

5. Summary

In this paper we presented ARTEMIS observations of sharp and transient mesoscale perturbations in plasma and magnetic field during a period of prolonged northward IMF (with substantial IMF B_y component), while the spacecraft were situated in the northern lobe of the magnetosphere at $X \sim -60\ R_E$. We then used global MHD simulations to help interpret these observations. Our key findings are the following:

1. Plasma and magnetic field parameters changed sharply and recovered within $\leq$10 min. Separation between two perturbations varied from approximately a few minutes to up to 30 min. The main characteristics of these perturbations are as follows: (1) enhancements in density and plasma pressure, (2) a drop in B_x and sometimes also a change in the B_x direction, (3) an enhancement in the tailward ($-V_x$) speed and quite often also a change in the V_y direction, and (4) the perturbations propagated tailward. The X scale of the perturbations is estimated to be ~10 R_E from simultaneous two-probe measurements.
2. The simulation shows that magnetospheric boundary exhibited significant oscillations accompanied by mesoscale vortical flows associated with the two K-H vortex modes. The inner mode vortex size is ~10 R_E in X and ~5 R_E in Y and Z. The inner mode vortical flow resulted in localized protrusions of the denser mantle plasma from the magnetopause to ~5 R_E inside the magnetosphere in the midtail, leading to localized plasma pressure and flow changes in the lobes. Accordingly, the magnetic field configuration changed to provide the $\mathbf{J} \times \mathbf{B}$ force to balance the enhanced flow shears and pressure gradients, and a B_x dip is formed as a result. The simulation results are repetitive, like the observations, and are qualitatively similar to the observed magnetic field and plasma variations at ARTEMIS, suggesting that such K-H protrusions are common and affect tail structure at and beyond the midmagnetotail.

Acknowledgments
We thank NSF GEM "Tail Environment and Dynamics at Lunar Distances" and "Modeling Methods and Validation" focus groups and NASA CCMC for hosting "Midtail Modeling Challenge" (https://ccmc.gsfc.nasa.gov/challenges/MidTail/). The work by Merkin has been supported by NASA grant NNX14AH77G. The ARTEMIS data are available for free and are with the Space Physics Environment Data Analysis System (SPEDAS) software (http://themis.igpp.ucla.edu/software.shtml). We acknowledge NASA contract NAS5-02099 for THEMIS and ARTEMIS, and C. W. Carlson and J. P. McFadden for the use of ESA data; K. H. Glassmeier, U. Auster, and W. Baumjohann for the use of FGM data provided under DLR contract 50-OC-0302. We thank J. H. King, N. Papatashvilli at AdnetSystems, NASA GSFC, and CDAWeb for providing the OMNI data.

References

Auster, H. U., et al. (2008), The THEMIS fluxgate magnetometer, *Space Sci. Rev.*, *141*, 235–264, doi:10.1007/s11214-008-9365-9.

Cassak, P. A., and S. A. Fuselier (2016), Reconnection at Earth's dayside magnetopause, in *Magnetic Reconnection: Concepts and Applications*, *Astrophys. and Space Sci. Lib.*, vol. 427, edited by W. Gonzalez and E. Parker, pp. 213–217, Springer Int. Publ., Switzerland.

Fedder, J. A., S. P. Slinker, J. G. Lyon, and R. D. Elphinstone (1995), Global numerical simulation of the growth phase and the expansion onset for substorm observed by Viking, *J. Geophys. Res.*, *100*, 19,083–19,093, doi:10.1029/95JA01524.

Gosling, J. T., D. N. Baker, S. J. Bame, E. W. Hones Jr., D. J. McComas, R. D. Zwickl, J. A. Slavin, E. J. Smith, and B. T. Tsurutani (1984), Plasma entry into the distant tail lobes: ISEE-3, *Geophys. Res. Lett.*, *11*, 1078–1081, doi:10.1029/GL011i010p01078.

Hasegawa, H., K. Maezawa, T. Mukai, and Y. Saito (2002), Plasma entry across the distant tail magnetopause: 1. Global properties and IMF dependence, *J. Geophys. Res.*, *107*(A5), 1063, doi:10.1029/2001JA900139.

Hasegawa, H., M. Fujimoto, T. D. Phan, H. Reme, A. Balogh, M. W. Dunlop, C. Hashimoto, and R. TanDokoro (2004), Transport of solar wind into Earth's magnetosphere through rolled-up Kelvin-Helmholtz vortices, *Nature*, *430*, 755–758, doi:10.1038/nature02799.

Hietala, H., J. F. Drake, T. D. Phan, J. P. Eastwood, and J. P. McFadden (2015), Ion temperature anisotropy across a magnetotail reconnection jet, *Geophys. Res. Lett.*, *42*, 7239–7247, doi:10.1002/2015GL065168.

Hietala, H., A. V. Artemyev, and V. Angelopoulos (2017), Ion dynamics in magnetotail reconnection in the presence of density asymmetry, *J. Geophys. Res. Space Physics*, *122*, 2010–2023, doi:10.1002/2016JA023651.

Hwang, K.-J., M. M. Kuznetsova, F. Sahraoui, M. L. Goldstein, E. Lee, and G. K. Parks (2011), Kelvin-Helmholtz waves under southward interplanetary magnetic field, *J. Geophys. Res.*, *116*, A08210, doi:10.1029/2011JA016596.

King, J. H., and N. E. Papitashvili (2005), Solar wind spatial scales in and comparisons of hourly Wind and ACE plasma and magnetic field data, *J. Geophys. Res.*, *110*, A02104, doi:10.1029/2004JA010649.

Li, L. Y., J. B. Cao, G. C. Zhou, T. L. Zhang, D. Zhang, I. Dandouras, H. Rème, and C. M. Carr (2011), Multiple responses of magnetotail to the enhancement and fluctuation of solar wind dynamic pressure and the southward turning of interplanetary magnetic field, *J. Geophys. Res.*, *116*, A12223, doi:10.1029/2011JA016816.

Li, W. Y., X. C. Guo, and C. Wang (2012), Spatial distribution of Kelvin-Helmholtz instability at low-latitude boundary layer under different solar wind speed conditions, *J. Geophys. Res.*, *117*, A08230, doi:10.1029/2012JA017780.

Lin, D., C. Wang, W. Li, B. Tang, X. Guo, and Z. Peng (2014), Properties of Kelvin-Helmholtz waves at the magnetopause under northward interplanetary magnetic field: Statistical study, *J. Geophys. Res. Space Physics*, *119*, 7485–7494, doi:10.1002/2014JA020379.

Lyon, J. G., J. A. Fedder, and C. M. Mobarry (2004), The Lyon-Fedder-Mobarry (LFM) global MHD magnetospheric simulation code, *J. Atmos. Sol. Terr. Phys.*, *66*, 1333–1350, doi:10.1016/j.jastp.2004.03.020.

Maezawa, K., and T. Hori (1998), The distant magnetotail: Its structure, IMF dependence, and thermal properties, in *New Perspectives on the Earth's Magnetotail*, *Geophys. Monogr. Ser.*, vol. 105, edited by A. Nishida, D. N. Baker, and S. W. H. Cowley, pp. 1–20, AGU, Washington, D. C.

McFadden, J. P., C. W. Carlson, D. Larson, V. Angelopoulos, M. Ludlam, R. Abiad, B. Elliott, P. Turin, and M. Marckwordt (2008), The THEMIS ESA plasma instrument and in-flight calibration, *Space Sci. Rev.*, *141*, 277–302, doi:10.1007/s11214-008-9440-2.

Merkin, V. G., and J. G. Lyon (2010), Effects of the low-latitude ionospheric boundary condition on the global magnetosphere, *J. Geophys. Res.*, *115*, A10202, doi:10.1029/2010JA015461.

Merkin, V. G., J. G. Lyon, and S. G. Claudepierre (2013), Kelvin-Helmholtz instability of the magnetospheric boundary in a three-dimensional global MHD simulation during northward IMF conditions, *J. Geophys. Res. Space Physics*, *118*, 5478–5496, doi:10.1002/jgra.50520.

Sibeck, D. G., and R.-Q. Lin (2014), Size and shape of the distant magnetotail, *J. Geophys. Res. Space Physics*, *119*, 1028–1043, doi:10.1002/2013JA019471.

Sibeck, D. G., et al. (2011), ARTEMIS science objectives, *Space Sci. Rev.*, *165*, 59–91, doi:10.1007/s11214-011-9777-9.

Taylor, M. G. G. T., et al. (2012), Spatial distribution of rolled-up Kelvin-Helmholtz vortices at Earth's dayside and flank magnetopause, *Ann. Geophys.*, *30*, 1025–1035, doi:10.5194/angeo-30-1025-2012.

Wang, C.-P., L. R. Lyons, and V. Angelopoulos (2014), Properties of low-latitude mantle plasma in the Earth's magnetotail: ARTEMIS observations and global MHD predictions, *J. Geophys. Res. Space Physics*, *119*, 7264–7280, doi:10.1002/2014JA020060.

Wiltberger, M., R. S. Weigel, W. Lotko, and J. A. Fedder (2009), Modeling seasonal variations of auroral particle precipitation in a global-scale magnetosphere-ionosphere simulation, *J. Geophys. Res.*, *114*, A01204, doi:10.1029/2008JA013108.